The Astrophysical Journal, 970:9 (11pp), 2024 July 20
https://doi.org/10.3847/1538-4357/ad4a77

Multiphase Black Hole Feedback and a Bright [C II] Halo in a LoBAL Quasar at $z\sim6.6$

Manuela Bischetti[1,2,19], Hyunseop Choi (최현섭)[3,4,19], Fabrizio Fiore[2,5], Chiara Feruglio[2,5], Stefano Carniani[6], Valentina D'Odorico[2,5,6], Eduardo Bañados[7], Huanqing Chen[8], Roberto Decarli[9], Simona Gallerani[6], Julie Hlavacek-Larrondo[3], Samuel Lai[10], Karen M. Leighly[11], Chiara Mazzucchelli[12], Laurence Perreault-Levasseur[3,4,13,14], Roberta Tripodi[2,5,15], Fabian Walter[7], Feige Wang[16], Jinyi Yang[16], Maria Vittoria Zanchettin[2,17], and Yongda Zhu[18]

[1] Dipartimento di Fisica, Universitá di Trieste, Sezione di Astronomia, Via G.B. Tiepolo 11, I-34131 Trieste, Italy; manuela.bischetti@units.it
[2] INAF—Osservatorio Astronomico di Trieste, Via G. B. Tiepolo 11, I-34131 Trieste, Italy
[3] Département de Physique, Université de Montréal, Succ. Centre-Ville, Montréal, QC H3C 3J7, Canada; hyunseop.choi@umontreal.ca
[4] Mila—Quebec Artificial Intelligence Institute, Montréal, QC, Canada
[5] IFPU—Institut for fundamental physics of the Universe, Via Beirut 2, 34014 Trieste, Italy
[6] Scuola Normale Superiore, Piazza dei Cavalieri 7, I-56126 Pisa, Italy
[7] Max Planck Institut für Astronomie, Königstuhl 17, D-69117, Heidelberg, Germany
[8] Canadian Institute for Theoretical Astrophysics, University of Toronto, 60 St George St., Toronto, ON M5R 2M8, Canada
[9] INAF—Osservatorio di Astrofisica e Scienza dello Spazio di Bologna, via Gobetti 93/3, I-40129, Bologna, Italy
[10] Research School of Astronomy and Astrophysics, Australian National University, Canberra, ACT 2611, Australia
[11] Homer L. Dodge Department of Physics and Astronomy, The University of Oklahoma, 440 W. Brooks St., Norman, OK 73019, USA
[12] Núcleo de Astronomía de la Facultad de Ingeniería, Universidad Diego Portales, Av. Ejército Libertador 441, Santiago, Chile
[13] Ciela—Montreal Institute for Astrophysical Data Analysis and Machine Learning, Montréal, QC, Canada
[14] Center for Computational Astrophysics, Flatiron Institute, 162 5th Avenue, New York, NY 10010, USA
[15] University of Ljubljana FMF, Jadranska 19, 1000, Slovenia
[16] Steward Observatory, University of Arizona, 933 N. Cherry Avenue, Tucson, AZ 85721, USA
[17] SISSA, Via Bonomea 265, 34136, Trieste, Italy
[18] Department of Physics & Astronomy, University of California, Riverside, Riverside, CA 92521, USA

Received 2024 March 12; revised 2024 April 18; accepted 2024 May 10; published 2024 July 15

Abstract

Although the mass growth of supermassive black holes during the epoch of reionization is expected to play a role in shaping the concurrent growth of their host galaxies, observational evidence of feedback at $z\gtrsim6$ is still sparse. We perform the first multiscale and multiphase characterization of black-hole-driven outflows in the $z\sim6.6$ quasar J0923+0402 and assess how these winds impact the cold gas reservoir. We employ the *SimBAL* spectral synthesis to fit broad absorption line features and find a powerful ionized outflow on a $\lesssim$210 pc scale, with a kinetic power ~2%–100% of the quasar luminosity. Atacama Large Millimeter/submillimeter Array (ALMA) observations of [C II] emission allow us to study the morphology and kinematics of the cold gas. We detect high-velocity [C II] emission, likely associated with a cold neutral outflow at ~0.5−2 kpc scale in the host galaxy, and a bright extended [C II] halo with a size of ~15 kpc. For the first time at such an early epoch, we accurately constrain the outflow energetics in both the ionized and the atomic neutral gas phases. We find such energetics to be consistent with expectations for an efficient feedback mechanism, and both ejective and preventative feedback modes are likely at play. The scales and energetics of the ionized and atomic outflows suggest that they might be associated with different quasar accretion episodes. The results of this work indicate that strong black hole feedback is occurring in quasars at $z\gtrsim6$ and is likely responsible for shaping the properties of the cold gas reservoir up to circumgalactic scales.

Unified Astronomy Thesaurus concepts: Broad-absorption line quasar (183); High-redshift galaxies (734); Galaxy evolution (594); Supermassive black holes (1663); Spectroscopy (1558); Interferometry (808); Submillimeter astronomy (1647); Near infrared astronomy (1093); Optical astronomy (1776); Warm ionized medium (1788); Circumgalactic medium (1879); Cold neutral medium (266)

1. Introduction

Bright quasars at $z\gtrsim6$ are powered by a billion solar-mass black holes (BHs) that lie well above the local BH mass −galaxy dynamical mass correlation (Neeleman et al. 2021), implying that BH growth dominates over galaxy growth during the first gigayear of the Universe (Volonteri 2012; Inayoshi et al. 2022; Hu et al. 2022). Cosmological simulations predict such a rapid BH growth to drive powerful winds at $z\sim6-7$ (Barai et al. 2018; van der Vlugt & Costa 2019). These winds are responsible for suppressing further BH growth and regulating star formation activity and the physical properties of the interstellar medium (ISM) and circumgalactic medium (CGM), possibly leading to the BH and host galaxy coevolution observed at lower redshift (Valentini et al. 2021; Pizzati et al. 2023; Costa et al. 2022). In recent years, a major effort has been undertaken to detect BH-driven winds from emission lines in the millimeter band, resulting in only a few detections and conflicting results about the occurrence and strength of cold gas outflows at $z\gtrsim6$ (e.g., Maiolino et al.

---

[19] Authors Bischetti and Choi contributed equally to the manuscript.

2012; Cicone et al. 2015; Bischetti et al. 2019a; Novak et al. 2020; Izumi et al. 2021; Tripodi et al. 2022; Meyer et al. 2022).

Recent deep spectroscopic surveys of quasars at $z \gtrsim 6$ showed that about half of the quasar population shows broad absorption line (BAL) features in the rest-frame UV spectrum, tracing ionized gas winds (Schindler et al. 2020; Bischetti et al. 2022, 2023; Yang et al. 2021), while at $z \lesssim 4$ the BAL quasar fraction is 10%–20% (Maddox et al. 2008; Gibson et al. 2009). BAL winds can arise in the nuclear regions of galaxies and, in $\gtrsim$50% of quasars, reach 0.1–10 kpc scale (Arav et al. 2018; Choi et al. 2022b); hence, they may represent a source of feedback on both BH and host galaxy growth. Outflow energetics have been measured with good accuracy in several BAL quasars at $z \lesssim 3$, finding indeed that BALs provide an efficient feedback mechanism (Fiore et al. 2017; Choi et al. 2020, 2022b; Miller et al. 2020). However, little is known about the gas physical properties and energetics of BALs in $z \gtrsim 6$ quasars.

Here we report on J0923+0402 ($z = 6.626$; Bischetti et al. 2022), which is the highest-redshift low-ionization BAL (LoBAL) quasar discovered so far. This object was initially classified as a low-luminosity, dust-reddened quasar based on Subaru/Hyper Suprime-Cam (HSC) and Wide-field Infrared Survey Explorer photometry (Matsuoka et al. 2018) but was revealed to be a brighter quasar with little extinction (Wang et al. 2019; Kato et al. 2020). Indeed, J0923+0402 has a bolometric luminosity $\log(L_{\rm Bol}/{\rm erg\ s^{-1}}) = 47.5$ and a BH mass $\log(M_{\rm BH}/M_\odot) = 9.4$ (Yang et al. 2021; Mazzucchelli et al. 2023), which imply that it is accreting close to the Eddington limit ($L_{\rm Bol}/L_{\rm Edd} \sim 1$, where $L_{\rm Edd}$ is the Eddington luminosity). The detection of strong C IV, Si IV, and Mg II absorption features associated with a BAL wind in J0923+0402 was reported in Bischetti et al. (2022, 2023). We exploit the *SimBAL* (Leighly et al. 2018) spectral analysis to measure the energetics of the BAL wind in J0923+0402. We also present ALMA observations of the [C II] $\lambda158\mu$m emission line to trace the galaxy-scale counterpart of the BAL wind and assess the impact of BH activity on ISM and CGM properties. Throughout the paper, we adopt a ΛCDM cosmology with $H_0 = 67.3$ km s^{-1}, $\Omega_\Lambda = 0.69$, and $\Omega_M = 0.31$ (Planck Collaboration et al. 2016).

2. Data Analysis and Results

2.1. *BAL Data and* SimBAL *Analysis*

We use the spectral-synthesis code *SimBAL* (Leighly et al. 2018) to fit the BAL features in the rest-UV spectrum of J0923+0402, which was acquired with the Very Large Telescope (VLT)/X-Shooter spectrograph as part of the XQR-30 survey (D'Odorico et al. 2023). Details on the data reduction and calibration are given in Bischetti et al. (2022) and D'Odorico et al. (2023). The spectrum was shifted to the rest frame using $z_{\rm [C\,II]}$ (Table 1, calculated as in Section 2.2) and binned to increase the signal-to-noise ratio (S/N $\gtrsim$ 5 per 100 km s^{-1} pixel in the C IV trough at ∼1500 Å). We fit the rest-frame spectral range 1280–2900 Å in which the main broad absorption features are observed.

Table 1
Properties of J0923+0402

Parameter	Value
R.A.	09:23:47.122
Decl.	+04:02:54.402
$z_{\rm [C\,II]}$	6.6321 ± 0.0003
$S_{\rm cont}$ (mJy)	0.80 ± 0.08
$S_{\rm [C\,II]}$ (Jy km s^{-1})	5.94 ± 0.35
FWHM$_{\rm [C\,II]}$ (km s^{-1})	400 ± 25
$L'_{\rm [C\,II]}$ ($10^9\ L_\odot$)	6.75 ± 0.45
BAL Outflow	
$v_{\rm max}$ (km s^{-1})	−32,000
$\log U$	$-0.32^{+0.01}_{-0.02}$
$\log N_{\rm H} - \log U^a$ (cm^{-2})	21.52 − 23.06
$\log a^a$	0.79 − 1.67
$\log(N_{\rm H}/[{\rm cm^{-2}}])^b$	$22.57^{+0.01}_{-0.02}$
$R_{\rm BAL}$ (pc)	3 − 210
$\log(\dot{M}_{\rm BAL}/[M_\odot\,{\rm yr^{-1}}])$	1.89 − 3.7
$\log(\dot{E}_{\rm BAL}/[{\rm erg\ s^{-1}}])$	45.69 − 47.51
$\log(\dot{P}_{\rm BAL}/[{\rm g\ cm\ s^{-2}}])$	36.81 − 38.62
[C II] Outflow	
$S_{\rm [C\,II]}$ (Jy km s^{-1})	0.40 ± 0.07
$v_{\rm [C\,II]}$ (km s^{-1})	-530 ± 30
$R_{\rm [C\,II]}$ (pc)	520 − 2, 220
$\log(\dot{M}_{\rm atom}/[M_\odot\,{\rm yr^{-1}}])$	2.18 − 2.81
$\log(\dot{E}_{\rm atom}/[{\rm erg\ s^{-1}}])$	43.11 − 43.76
$\log(\dot{P}_{\rm atom}/[{\rm g\ cm\ s^{-2}}])$	35.85 − 36.51

Notes. R.A. and decl. refer to the peak of the 242–257 GHz continuum. Uncertainties correspond to a 68% confidence level for the [C II] outflow properties and to 95% for those of the BAL outflow. The ranges of outflow radii and energetics correspond to the plausible range of locations of the outflowing gas (Section 3.1).

[a] The range of values extracted from the multiple velocity bins is reported.

[b] Corrected for the covering fraction (Appendix A.1).

We use a velocity-resolved model for the BAL absorption features (Leighly et al. 2018; Choi et al. 2020) to fit the broad opacity profile observed in J0923+0402. We consider 25 bins with velocities spanning from ∼−32,000 to ∼−6800 km s^{-1}.[20] Each bin is ∼1000 km s^{-1} wide, which is sufficient to model the velocity profile of the troughs observed in the X-Shooter data while avoiding overfitting the BAL features. The wind properties (e.g., column density, mass outflow rate) were calculated from the sum of the values calculated for each velocity bin. The version of *SimBAL* used in this work uses the grids calculated from version C17 of CLOUDY (Ferland et al. 2017), which assumes solar metallicity and spectral energy distribution (SED) of an ionizing spectrum that is suitable for luminous quasars (see Leighly et al. 2018; Choi et al. 2020, 2022b, for a discussion of the *SimBAL* updates). To model the unabsorbed quasar emission, we used the composite template spectrum from Bischetti et al. (2023). We fitted the rest-frame spectral range 1280–2900 Å in which the main broad absorption features are observed.

We consider a single ionization parameter ($\log U$), while column density (parameterized as $\log N_{\rm H} - \log U$) and partial covering parameter ($\log a$) were allowed to vary across different bins. As the X-Shooter data show no BAL features associated with transitions sensitive to gas density (e.g., Lucy et al. 2014), we did not include density as a free parameter in the *SimBAL* modeling. Instead, we fixed the density at $\log(n/{\rm cm^{-3}}) = 6$ and verified that the best-fit parameters do not significantly change ($\lesssim$0.15 dex) considering the large range of densities $2.8 \lesssim \log(n/{\rm cm^{-3}}) \lesssim 8$ typically measured for

---

[20] We retain the signs for the velocities as calculated from the quasar rest frame and compare their magnitudes (i.e., −10,000 km s^{-1} is a "lower" velocity than −30,000 km s^{-1}; e.g., Choi et al. 2022a).

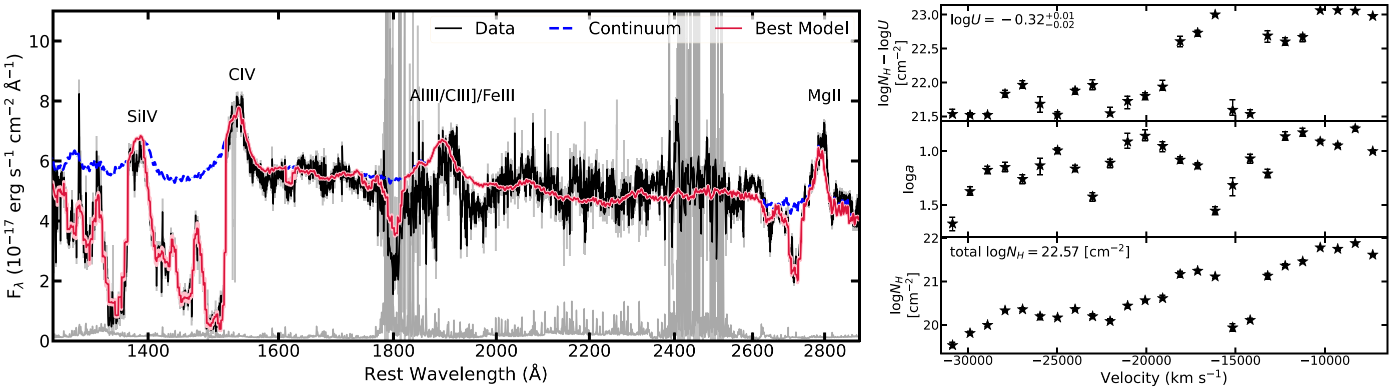

Figure 1. Left: X-Shooter spectrum of J0923+0402 (black) and best-fitting *SimBAL* model (red). The dashed blue curve represents the unabsorbed quasar emission model by Bischetti et al. (2023). The noise spectrum and the spectral regions excluded from the fit are plotted in gray. Labels indicate the major UV emission lines. Right: BAL outflow physical parameters as a function of velocity, with error bars representing 95% confidence regions. The top two panels show the fit parameters ($\log U$, $\log N_{\rm H} - \log U$, $\log a$) used in *SimBAL* modeling. The bottom panel shows the distribution of hydrogen column density ($\log N_{\rm H}$) corrected for the covering fraction (Appendix A.1).

LoBALs and FeLoBALs[21] (Leighly et al. 2018; Choi et al. 2022b). These variations are indeed small compared to the ranges of outflow energetics we calculate in Section 3.1.

The best-fit model is shown in Figure 1. Overall, we find an excellent agreement between the model and spectrum, the sole discernible deviation in Al III absorption, which falls within a region heavily affected by strong tellurics. We obtain a robust constraint of the ionization parameter of the BAL gas with $\log U = -0.32^{+0.01}_{-0.02}$, thanks to the presence of BAL transitions from both low-ionization ions (e.g., Al III, Mg II) and high-ionization ions (e.g., C IV). We find that the bulk of the column density is concentrated at the lower velocities (Figure 1, right panel). This trend is reflected in the observed BAL structures, in which the LoBAL transitions are found only at the low-velocity end ($v_{\rm out} \gtrsim -13{,}000\,{\rm km\,s^{-1}}$; Figure 5). The total hydrogen column density of the outflow $\log(N_{\rm H}/{\rm cm^{-2}}) = 22.57^{+0.01}_{-0.02}$ was derived by correcting the column densities for partial covering (Appendix A.1) and summing over all bins.

The covering fraction parameter $\log a$ also varies greatly with velocity. The shape of the C IV trough roughly matches the velocity structure of $\log a$ (low covering corresponds to high values of a; see Leighly et al. 2019). This is because the line profile of a saturated BAL is highly dependent on the properties of partial covering (e.g., de Kool et al. 2002). Our best-fitting model suggests that the BAL profile is produced by a combination of change in column density and partial covering across the velocity rather than by gas ionization structure, given that a single ionization parameter model is sufficient to recreate the profile. Uncertainties were calculated from the posterior probability distribution of model parameters. Further details on the *SimBAL* modeling of J0923+0402 can be found in Appendix A.1.

2.2. ALMA Data

We analyze archival Atacama Large Millimeter/submillimeter Array (ALMA) observations of J0923+0402 from projects 2018.1.01188S, 2019.1.00111S, and 2021.1.00934S. These data sets target [C II] ($\nu_{\rm rest} = 1900.5369$ GHz) and band 6 continuum emission (observed frequency ∼242−257 GHz) with angular resolution varying from ∼0.″12 to 0.″57. Visibilities were calibrated using the standard calibration provided by the ALMA observatory and the default phase, bandpass, and flux calibrators. To maximize the sensitivity and, at the same time, improve the sampling of the *u*-*v* plane, we merged the visibilities from the three data sets. We created continuum maps by averaging visibilities over all four 1.875 GHz spectral windows, excluding the spectral range covered by [C II] emission. To model and subtract the continuum emission to the line, we combined the adjacent spectral windows in the baseband containing [C II] and performed a fit in the *u*-*v* plane to channels with $|v| > 750$ km s^{-1}, using a first-order polynomial continuum. Continuum-subtracted data cubes were created using CASA task *tclean*, with the *hogbom* cleaning algorithm in noninteractive mode, a threshold equal to two times the rms sensitivity, and a natural weighting of the visibilities. For [C II] data cubes, we adopted a 30 km s^{-1} channel width. The resulting synthesized beam is $0.''16 \times 0.''15$ for the spectral window including [C II] (rms sensitivity 7.8×10^{-5} Jy beam^{-1} for a 30 km s^{-1} channel width) and $0.''14 \times 0.''13$ for the continuum image (rms sensitivity 5.9×10^{-6} Jy beam^{-1}).

We detect a bright [C II] emission, with a velocity-integrated flux density of $S_{\rm [C\,II]} \simeq 6.1$ Jy km s^{-1}, corresponding to a luminosity $L_{\rm [C\,II]} \simeq 6.7 \times 10^9\,L_\odot$. The [C II] spectrum extracted from the 3σ isophote contours is shown in the middle panel of Figure 2. The peak of the [C II] emission is located at an observed frequency of 249.019 GHz, corresponding to a $z_{\rm [C\,II]} = 6.6321$, which is similar to the [C II]-based redshift previously reported by Yang et al. (2021; the difference is less than one channel of our ALMA data cube). Fitting a 2D Gaussian to the [C II] map gives an FWHM size of 1.28×0.92 arcsec^2, which is about 7.1×5.1 kpc^2. We also detect the ∼242−257 GHz continuum emission (Figure 2, right panel) with a flux density $S_{\rm cont} \simeq 0.8$ mJy (Table 1). This corresponds to an infrared luminosity $L_{\rm IR,8-1000\mu m} \simeq 2.4 \times 10^{12}\ L_\odot$, assuming a typical dust temperature of 47 K and a dust emissivity index $\beta = 1.6$ of high-redshift quasar host galaxies (Beelen et al. 2006; Tripodi et al. 2023). The continuum morphology shows a main peak close to the quasar optical position, based on JWST NIRCam observations (F200W filter, project GO 2078, black cross in Figure 2). We measure a 0.″13 offset with respect to the quasar position from Subaru/HSC observations (Kato et al. 2020) and do not find evidence for astrometric errors in the HSC image, although we caution that

---

[21] LoBAL quasars that also show broad absorption associated with Fe II transitions.

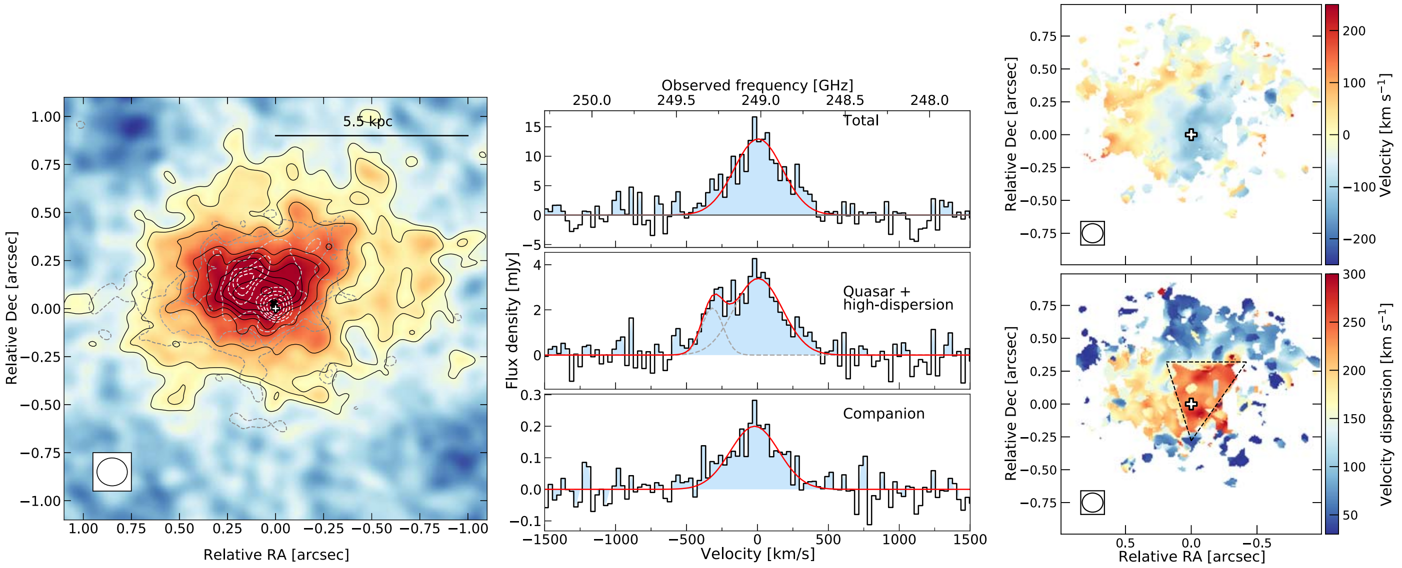

Figure 2. Left: map of the [C II] emission in J0923+0402. Solid contours correspond to [3, 4, 6, 8, 10, 12, 13]σ significance, where $\sigma = 0.017$ Jy beam^{-1} km s^{-1}. The same levels are shown for the continuum emission by the dashed contours, with $\sigma = 5.9 \times 10^{-6}$ Jy beam^{-1}. The black cross indicates the quasar optical position, as measured from NIRCam F200W data, and the white plus sign corresponds to the peak of the 242–257 GHz continuum emission probed by ALMA. Middle: [C II] spectrum corresponding to the total emission detected at $\gtrsim 3\sigma$ (upper panel). The best-fit Gaussian profile is shown by the red curve. The central panel displays the [C II] spectrum extracted from the region with velocity dispersion higher than 230 km s^{-1}, including the quasar location. To model the line profile, we added a second blueshifted Gaussian component with $v \simeq -300$ km s^{-1} to the scaled best-fit model of the top panel. The lower panel shows the [C II] spectrum extracted from one beam aperture centered on the secondary continuum peak. Right: velocity and velocity dispersion maps corresponding to the [C II] emission at $>3\sigma$. The black dashed polygon highlights the triangle-shaped region with high velocity dispersion (Section 2.2).

the size of an HSC pixel is 0.″17. We also detect a second continuum peak east of the main one, separated by $\simeq$1.2 kpc, possibly indicating a companion galaxy. Due to the presence of diffuse emission between and around these continuum peaks, it is not straightforward to derive a continuum flux ratio between the quasar host galaxy and the companion. We provide a basic estimate by independently fitting a 2D Gaussian profile to the two continuum peaks and find a quasar-to-companion flux ratio of $\sim$2.5: 1. The maximum of the [C II] emission is located between these two continuum peaks, about $\simeq$550 pc offset from the main one.

Figure 2 right shows the velocity and velocity dispersion maps of the [C II] emission J0923+0402. We do not find a strong velocity gradient close to the quasar location, as the bulk of [C II] shows projected velocities within ± 100 km s^{-1}. This suggests that the quasar host galaxy is seen under relatively low inclination, as typically expected for BAL quasars (e.g., Elvis 2000). Moderately redshifted emission is detected $\sim$3 kpc east from the nucleus, in a region in which we also find extended continuum emission, likely due to a tidal feature. We also find blueshifted velocities at the location of the quasar and in a triangle-shaped region, extending up to 0.″4 from it. Such velocities are due to a second peak in the [C II] spectrum, blueshifted by $v \simeq -300$ km s^{-1} with respect to the systemic emission and reaching $v \simeq -500$ km s^{-1} (Figure 2 middle). The [C II] velocity dispersion is generally high ($\sigma_v \simeq 150$ 200 km s^{-1}) in the central 1.5–2 kpc, the highest values ($\simeq$300 km s^{-1}) being also located in the triangle-shaped region. The combination of high velocity and high velocity dispersion suggests the presence of a [C II] outflow in the host galaxy of J0923+0402. Due to the moderate velocities observed, we cannot a priori exclude that the triangle-shaped region is associated with a tidal feature. However, as high-velocity ($v < -250$ km s^{-1}) [C II] emission is very faint at the location of the companion galaxy (Figure 2, middle panel) and is instead mostly located northwest from the quasar (Figure 2, right panel, and Figure 7), we deem it unlikely that this emission is due to the merger traced by the continuum emission. The peak of this blueshifted emission is located about 0.″1 (520 pc) from the nucleus, and its flux is about 7% of the total [C II] flux (Table 1), similar to what was previously measured for other [C II] outflows at $z \gtrsim 6$ (e.g., Bischetti et al. 2019a; Izumi et al. 2021).

3. Discussion and Conclusions

3.1. Wind Location and Energetics

We determine the plausible range of BAL wind radii 3 pc $\lesssim R_{\rm BAL} \lesssim 210$ pc based on the assumption that the BAL outflow energy does not exceed $L_{\rm Bol}$ (upper limit) and by assuming that the density of the BAL absorbing gas is lower than that of gas located in the quasar broad-line region (BLR), consistent with previous measurements of BAL physical properties and energetics from $z < 3$ quasars (Appendix A.2). We calculate the mass outflow rate from the best-fit $N_{\rm H}$ and v using Equation (9) in Dunn et al. (2010), which adopts a thin-shell geometry, and assuming a mean molecular weight $\mu = 1.4$ and a global covering $\Omega = 0.2$ (e.g., Hewett & Foltz 2003). The latter is derived from the fraction of BAL quasars at $z \lesssim 4$. For $z \sim 6$ quasars, the frequency increases to almost 50% (Bischetti et al. 2022), which may suggest a global covering fraction as high as 0.5, which would yield a higher estimate of the mass outflow rate. Based on the range of BAL wind radii, we measure a mass outflow rate $1.9 \lesssim \log(\dot{M}_{\rm BAL}/M_\odot\,{\rm yr}^{-1}) \lesssim 3.7$ (Table 1), which is is among the largest values measured for BAL winds in quasars at $z \lesssim 3$ (Choi et al. 2020, 2022b; Miller et al. 2020; Bruni et al. 2019; Vietri et al. 2022; Figure 3, left panel). Similarly, we calculated the total mass of the BAL wind to be in the range $4.0 \lesssim \log(M_{\rm BAL}/M_\odot) \lesssim 7.7$, considering a shell-like scenario. The kinetic power and momentum flux of the BAL wind are listed in Table 1.

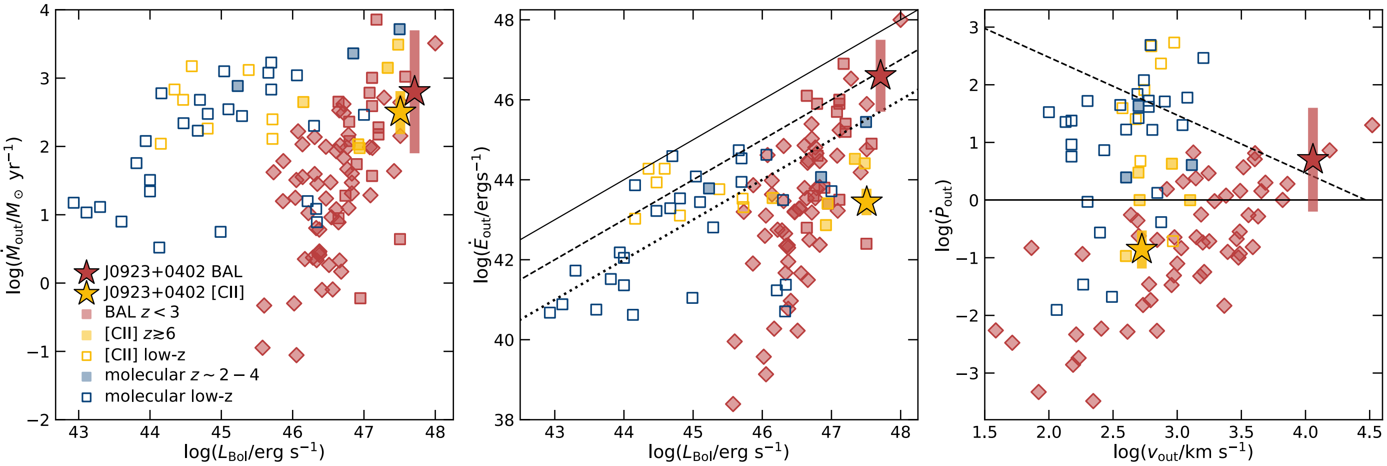

Figure 3. Left: mass outflow rate as a function of bolometric luminosity for the [C II] and BAL outflow detected in J0923+0402 (stars). The shaded bars show the range of possible values according to our analysis. We compare our results with [C II] outflows from Bischetti et al. (2019a), Izumi et al. (2021), and Tripodi et al. (2022) and BAL outflows from Choi et al. (2020, 2022b; diamonds) and Miller et al. (2020; squares). We also include the compilation of BH-driven molecular outflows from Bischetti et al. (2019b, and references therein) and recent measurements by Ramos Almeida et al. (2022) and Zanchettin et al. (2021, 2023). The estimates for the comparison BAL outflows were also calculated assuming a thin-shell scenario. The bolometric luminosity for the BAL outflow of J0923+0402 is arbitrarily shifted for plotting. Middle: outflow kinetic power as a function of $L_{\rm Bol}$. The solid, dashed, and dotted lines correspond to $L_{\rm Bol}$, $0.1L_{\rm Bol}$, and $0.01L_{\rm Bol}$, respectively. Right: outflow momentum flux as a function of the outflow velocity. The solid (dashed) line indicates the expected momentum boost for a BH-driven wind arising with nuclear velocity 0.1c and propagating with a momentum-conserving (energy-conserving) expansion (Zubovas & King 2012).

For the putative [C II] outflow in J0923+0402, we calculate an atomic gas mass $M_{\rm atom} \simeq 4.3 \times 10^8\ M_\odot$ using Equation (1) in Hailey-Dunsheath et al. (2010) and typical assumptions on the physical conditions of the [C II]-emitting gas. We assume a C$^+$ abundance of 1.4×10^{-4} per hydrogen atom and a gas temperature of 200 K (Kaufman et al. 1999; Hailey-Dunsheath et al. 2010). Indeed, a temperature of a few hundred kelvin is expected in the outflow even in the molecular gas phase (Richings & Faucher-Giguère 2018). A temperature in the range 100–1000 K would imply a variation of only 20% in $M_{\rm atom}$. As we do not know the gas density in the [C II] outflow, we consider the density limit $n \gg n_{\rm crit}$, where $n_{\rm crit} = 2.7 \times 10^3$ cm^{-3} is the [C II] critical density, to derive a lower limit to the outflowing gas mass (Bischetti et al. 2019a). This limit is consistent with the large density ($n \simeq 10^5$ cm^{-3}) measured in the host galaxy of the $z\sim6$ quasar J1148 + 5251 by Maiolino et al. (2005) and with the large densities found in several quasar outflows (Aalto et al. 2012, 2015). A lower gas density (e.g., Meyer et al. 2022) might be expected for a kiloparsec-scale outflow and would correspond to a higher mass of the [C II] outflow.

We compute the [C II] mass outflow rate using Equation (1) in Bischetti et al. (2019b) for a shell-like outflow geometry (Lutz et al. 2020; Izumi et al. 2021). To account for the uncertainty on the [C II] outflow location, we consider either the maximum extent or the scale of the bulk of the high-velocity [C II] emission (Section 2.2). This results in $\dot{M}_{\rm atom} \simeq 150 - 640\ M_\odot$ yr^{-1}, similar to what has been previously reported for [C II] outflows detected at $z \gtrsim 6$ in a few individual quasars or via stacking analysis (Maiolino et al. 2012; Cicone et al. 2014; Izumi et al. 2021; Tripodi et al. 2022; Bischetti et al. 2019a) and in low-redshift active galactic nuclei with Herschel/SPIRE observations (Janssen et al. 2016). We calculate the kinetic power of the BAL and [C II] outflows as $\dot{E} = \dot{M}v^2/2$ and the outflow momentum load $\dot{P} = \dot{M}v/(L_{\rm Bol}/c)$, which is the outflow momentum flux normalized to the quasar radiation momentum flux (Table 1).

3.2. Multiphase and Multiscale Outflow

J0923+0402 shows evidence of a relatively compact ($\lesssim$210 pc) BAL wind of ionized gas and of a neutral atomic outflow extending up to galactic scale (520−2200 pc). The [C II] outflow is more extended than the BAL, but if we consider the upper limit on $R_{\rm BAL}$, their sizes are in order-of-magnitude agreement. Most of the outflowing gas mass is carried by the neutral outflow ($10 \lesssim M_{\rm atom}/M_{\rm BAL} \lesssim 4 \times 10^4$), similar to the findings for low-redshift active galactic nuclei (Fluetsch et al. 2019; Speranza et al. 2023). The mass outflow rates for the two outflow phases are roughly similar (Figure 3, left panel), while the bulk of the outflow luminosity is associated with the ionized phase, as the BAL kinetic power is consistent with a significant, if not a major, fraction of the quasar luminosity ($0.02 \lesssim \dot{E}_{\rm BAL}/L_{\rm Bol} \lesssim 1.0$; Figure 3, middle panel). Such a high luminosity matches the expectations for an efficient quasar feedback mechanism (e.g., Faucher-Giguère & Quataert 2012; Costa et al. 2014) and supports the scenario previously suggested by Bischetti et al. (2022, 2023) in which BAL quasars witness strong quasar feedback occurring at $z \gtrsim 6$. The mass outflow rate of the BAL wind is larger than the mass accretion rate necessary to power the observed quasar luminosity, assuming a standard 10% accretion efficiency (57 $M_\odot$ yr^{-1}; Marconi et al. 2004). This implies that quasar feedback will likely suppress further BH growth. Despite hosting such a powerful BAL, J0923+0402 shows at most a mild perturbation of the cold gas kinematics in its central region, as only modest [C II] velocities are observed. A possible explanation for this might be that the BAL imprint on the ISM kinematics is diluted by the modest resolution (∼800 pc) of the ALMA observations. This may imply a small coupling of the ionized gas in the outflow with the [C II] gas, especially if the bulk of [C II] is coming from photodissociated regions (PDRs). It could also be interpreted as the BAL having a small impact on the ISM because of the relatively low opening angle of the wind (e.g., Menci et al. 2019; Bischetti et al. 2019a).

Concerning possible driving mechanisms of the outflows in J0923+0402, we find $\dot{P} < 1$ for the atomic phase (Figure 3, right panel), while models of quasar outflows based on the energy-driven expansion of a radiatively driven nuclear wind predict load factors $\gg$10 (Faucher-Giguère & Quataert 2012; Zubovas & King 2012). Differently, if the BAL wind is located on scales $\gtrsim$10 pc, its momentum load is large enough to be in agreement with an energy-conserving expansion. This difference between the neutral and ionized outflows in J0923+0402 suggests that the two outflows might not be associated with the same accretion episode. The flow timescales ($\tau \sim R/v$) of the outflows are also very different, $\tau_{\rm BAL} \lesssim 1.4 \times 10^4$ yr and $\tau_{\rm atom} \simeq (1-4) \times 10^6$ yr, respectively. While the BAL is likely powered by the observed $L_{\rm Bol}$, the [C II] outflow might be a remnant from a previous accretion episode, similar to the fossil outflows discovered in low-redshift active galactic nuclei (Fluetsch et al. 2019; Bischetti et al. 2019b; Zubovas & Maskeliūnas 2023). Multiple episodes of strong quasar feedback, spaced out by phases of gas accretion due to mergers or inflows from the intergalactic medium, are indeed expected by cosmological simulations of high-redshift quasars (e.g., van der Vlugt & Costa 2019; Zubovas & King 2021).

From FWHM$_{\rm [C\,II]}$ (Table 1) we can derive a rough estimate of the dynamical mass using Equation (14) in Neeleman et al. (2021) and, in turn, of the escape velocity within the inner ~2 kpc, which is $v_{\rm esc} \simeq 500$ km s^{-1}. As the velocity of the [C II] outflow is similar to $v_{\rm esc}$, a significant fraction of the outflowing gas might be able to reach CGM scales in a few megayears. The feedback mechanism occurring in J0923+0402 thus likely involves both channels of the quasar feedback paradigm, preventative and ejective (e.g., Somerville & Davé 2015; Curtis-Lake et al. 2023). While the neutral outflow can displace or remove gas from the host galaxy, the ionized wind injects large amounts of energy into the ISM and CGM, thereby reducing the accretion of gas at later epochs (Tumlinson et al. 2017).

3.3. Bright [C II] Halo: Is There a Link to Feedback?

ALMA observations of J0923+0402 reveal the presence of a bright [C II] emission associated with the host galaxy ISM and CGM. [C II] mostly traces neutral atomic gas in PDRs and is often used as a tracer of star formation in high-redshift galaxies (Maiolino et al. 2005; Decarli et al. 2018), although it can be also emitted from the partly ionized medium (Carilli & Walter 2013; Lagache et al. 2018). In the case of J0923+0402, the [C II] luminosity is ~0.6 dex brighter than what is typically observed in quasars with similar $L_{{\rm IR},8-1000\mu{\rm m}}$ (Decarli et al. 2018; Venemans et al. 2020), suggesting that a significant fraction of its [C II] emission may not arise from PDRs but may rather trace diffuse and ionized gas in the CGM. This is supported by the very different morphology of continuum and [C II] emission (Figure 2) and by about 50% of the [C II] emission arising beyond a radius of $\simeq$3.3 kpc (Figure 4).

[C II] emission on scales beyond a few kiloparsecs has been previously detected by stacking samples of star-forming galaxies at $z \gtrsim 5$ and in a few individual targets (Fujimoto et al. 2019, 2020; Ginolfi et al. 2020a; Herrera-Camus et al. 2021; Akins et al. 2022; Lambert et al. 2023). Systematic studies in $z \gtrsim 6$ quasars have instead found that typical [C II] radii are <2 kpc (Novak et al. 2020; Venemans et al. 2020) and that the upper envelope of these values is often associated with recent/ongoing mergers (Neeleman et al. 2021). Radii >3 kpc have been reported in only a few cases, based on moderate-resolution observations ($0''.5-1''$; Cicone et al. 2015; Izumi et al. 2021). We calculate the brightness profile of [C II] emission in J0923+0402 in circular annuli of $0''.15$ radius, following the method described in Tripodi et al. (2022), and find that the size of the [C II] halo around J0923+0402 is four times more extended than the stacked [C II] profile by Novak et al. (2020), and it is also larger than the stacked halo of massive galaxies obtained by Fujimoto et al. (2019) after removing possible active galaxies in their sample.

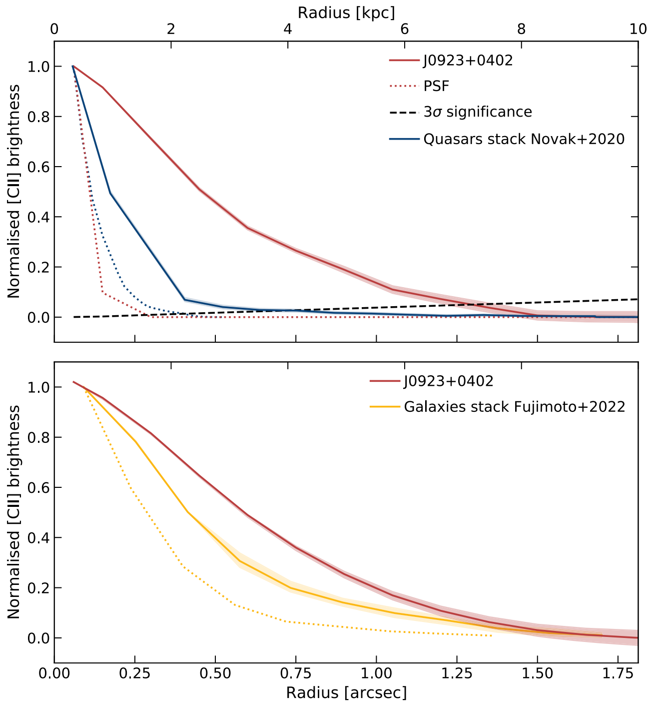

Figure 4. Top: brightness profile of the [C II] emission in J0923+0402 (red solid curve) and normalized to the maximum value. The brightness profile associated with the ALMA point-spread function (PSF) is shown by the dotted red curve, while the dashed curve shows the profile associated with the 3σ level. The [C II] stacked profile of $z \sim 6$ quasar hosts, including mergers, by Novak et al. (2020) is shown for comparison (PSF ~ $0''.18$). Shaded areas indicate 68% confidence level uncertainties. Bottom: comparison of the [C II] brightness profile of J0923+0402 and the stacked profile of massive star-forming galaxies by Fujimoto et al. (2019). We convolved our data to the PSF ~ $0''.4$ by Fujimoto et al. (2019) to compare sizes for a similar angular resolution.

Although J0923+0402 likely has a merging companion located ~1 kpc eastward from the nucleus, the morphology of the [C II] emission is mostly symmetric (the east–west vs. north–south size ratio is ~1.2, considering the 3σ contours in the left panel of Figure 2) and extends to much larger radii. This is different from what is typically observed via [C II] in merging systems, that is, a [C II] bridge connecting quasar and companion, instead of a diffuse halo (e.g., Tripodi et al. 2024; Decarli et al. 2019). The fact that mergers typically modify the [C II] morphology along a specific direction is also supported by the fact that Novak et al. (2020) do not find a difference in the [C II] stacked profiles of $z \sim 6$ quasars with/without mergers. The above picture questions the merger as the main mechanism responsible for the extended [C II] halo (e.g., Ginolfi et al. 2020b; Lambert et al. 2023). An alternative scenario concerns [C II] emission being powered when streams of dense and cold gas accrete on high-redshift galaxies and are heated owing to gravitational energy release and shock heating (e.g., Dekel et al. 2009). However, in such a scenario, the metallicity of the inflowing gas is expected to be low and not to significantly contribute to [C II] emission (Pallottini et al. 2014; Vallini et al. 2015).

Recent works have suggested a link between feedback and extended gaseous halos around $z\sim6$ star-forming galaxies. Given the high luminosity and the evidence of multiple outflow episodes in J0923+0402, such a scenario might explain its extended [C II] emission. On one hand, feedback is able to displace gas beyond a few kiloparsecs (Costa et al. 2019; Vito et al. 2022), and at the same time, outflows can significantly contribute to gas heating via shocks (Appleton et al. 2013; Fujimoto et al. 2020; Pizzati et al. 2023). If this is the case for J0923+0402, the [C II] halo could be a remnant of past feedback activity (Pizzati et al. 2023), as we do not currently observe emission from high-velocity gas on the CGM scale. On the other hand, BH feedback can regulate the fraction of photons reaching the scales of the CGM (Costa et al. 2022). Along the lines of sight with high escape fraction (e.g., those cleared out by the BAL wind), the halo would be mostly ionized (e.g., Obreja et al. 2024), consistent with the Lyα halos frequently detected around $z\gtrsim6$ quasars (Farina et al. 2019). If the global escape fraction remains relatively low (Stern et al. 2021), extended and bright [C II] halos are expected in massive halos such as those of $z\gtrsim6$ quasars (Pizzati et al. 2023; Costa 2023).

The high redshift of J0923+0402 implies that Lyα emission lies at the very edge of the MUSE spectral band, thus severely challenging the detection of a Lyα halo around this quasar. Cycle 3 JWST observations with NIRSpec Integral Field Unit will allow us to investigate the possible presence of companion galaxies not detected by ALMA and map the morphology and kinematics of the warm ionized gas phase in the host galaxy and up to the CGM of J0923+0402, as traced by the Hα and [O III] emission lines (e.g., Leibler et al. 2018; Marshall et al. 2023).

Acknowledgments

We thank Kastitis Zubovas and Tiago Costa for valuable suggestions during the preparation of this manuscript. This paper makes use of the following ALMA data: ADS/JAO. ALMA#2018.1.01188S (P.I. F. Wang), ADS/JAO. ALMA#2019.1.00111S (P.I. B. Venemans), and ADS/JAO. ALMA#2021.1.00934S (P.I. J, Yang). ALMA is a partnership of ESO (representing its member states), NSF (USA), and NINS (Japan), together with NRC (Canada), MOST and ASIAA (Taiwan), and KASI (Republic of Korea), in cooperation with the Republic of Chile. The Joint ALMA Observatory is operated by ESO, AUI/NRAO and NAOJ. This work is based in part on observations made with the NASA/ESA/CSA James Webb Space Telescope. The JWST data presented in this article were obtained from the Mikulski Archive for Space Telescopes (MAST) at the Space Telescope Science Institute. The specific observations analyzed can be accessed via doi:10.17909/npbb-0x08. These observations are associated with program GO 2078 (P.I. F. Wang). The project leading to this publication has received support from ORP, which is funded by the European Union's Horizon 2020 research and innovation program under grant agreement No. 101004719 [ORP]. M.B. acknowledges support from INAF project 1.05.12.04.01—MINI-GRANTS di RSN1 "Mini-feedback" and from UniTs under FVG LR 2/2011 project D55-microgrants23 "Hyper-gal." M.B., C.F., and F.F. acknowledge support from INAF PRIN 2022 2022TKPB2P—BIG-z. Some of the computing for this project was performed at the OU Supercomputing Center for Education & Research (OSCER) at the University of Oklahoma (OU). J.H.-L. acknowledges the Canada Research Chair program, the NSERC discovery grant, and the Discovery Accelerator Supplements program.

Facility: ALMA, VLT(X-Shooter), Subaru(HSC), JWST (NIRCam).

Software: astropy (Astropy Collaboration et al. 2013, 2018, 2022), CLOUDY (Ferland et al. 2017), SimBAL (Leighly et al. 2018).

Appendix A
SimBAL Analysis

Before performing the *SimBAL* analysis, we identified the data points and the regions in the VLT/X-Shooter data to be excluded in the spectral modeling. We masked the pixels heavily affected by telluric features by identifying any data points with an S/N < 3. Deep narrow intervening absorption lines at $\lambda\sim1550$ Å, identified as Mg II $\lambda\lambda$2796, 2803 at $z_{\rm abs}=3.163$ (Davies et al. 2023), were also masked.

A.1. *Best-fit* SimBAL *Model*

SimBAL fits both the continuum and absorption simultaneously to obtain a robust solution (e.g., Choi et al. 2020, 2022b). *SimBAL* requires six physical parameters to create synthetic BAL features for a given outflow: the dimensionless ionization parameter $\log U$, the gas density $\log n$ [cm^{-3}], a column density parameter $\log N_{\rm H}-\log U$ [cm^{-2}] that represents a hydrogen column density normalized by ionization parameter, the velocity offset $v_{\rm off}$(km s^{-1}), the width of the absorption lines $v_{\rm width}$ (km s^{-1}), and a dimensionless covering fraction parameter $\log a$. The inhomogeneous partial covering model is adopted in *SimBAL*, in which a power-law distribution of opacity ($\tau=\tau_{\rm max}x^{a}$ and $x\in(0,\ 1)$; Sabra & Hamann 2005; Arav et al. 2005) is controlled by $\log a$. The full covering is achieved with low values of a close to 0, and larger a (or $\log a$) represents the low partial covering of the emission source. Further discussion of inhomogeneous partial covering is given in Leighly et al. (2019).

We used the *SimBAL* version introduced in Choi et al. (2020), which uses an ionic column density grid calculated for a solar-metallicity gas. We expect that a higher-metallicity grid would result in a smaller column density roughly inversely proportional to the metal enhancement factor and, therefore, weaker outflow strengths. For instance, Leighly et al. (2018) found in their analysis of LoBAL SDSS J0850 + 4451 that a 3 times higher metallicity grid would result in a smaller column density by a factor of about 3. We used a set of 25 velocity-adjacent top-hat bins (top-hat accordion model; Leighly et al. 2018) to model the absorption features. The number of bins has a negligible impact on the result of the *SimBAL* analysis unless it is set too low or high (Leighly et al. 2018). The bin width of $\sim$1000 km s^{-1} proved to be sufficient to fit the BAL velocity structure observed in the binned X-Shooter data that we used for the *SimBAL* analysis.

We extracted velocity-resolved physical properties from the best-fit *SimBAL* model (Figure 1) and the total column density of the outflowing gas to calculate the wind energetics (Section 3.1). The best-fitting model presented in this work assumes a constant ionization parameter across the velocities.

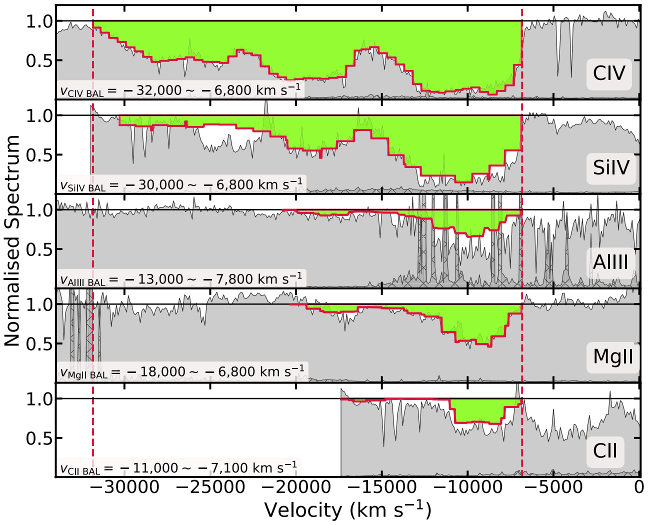

Figure 5. The normalized spectra of the X-Shooter data (gray shaded areas) and *SimBAL* model (red curve, green shaded areas) plotted in the quasar rest-frame velocity. The dashed vertical lines highlight the maximum and minimum velocities of the BAL outflow. The C IV BAL represents the widest trough, and the LoBALs show significantly smaller velocity widths compared to the HiBAL troughs. We found that both HiBALs and LoBALs have similar minimum outflow velocities. The hatched gray area indicates the uncertainties associated with the data.

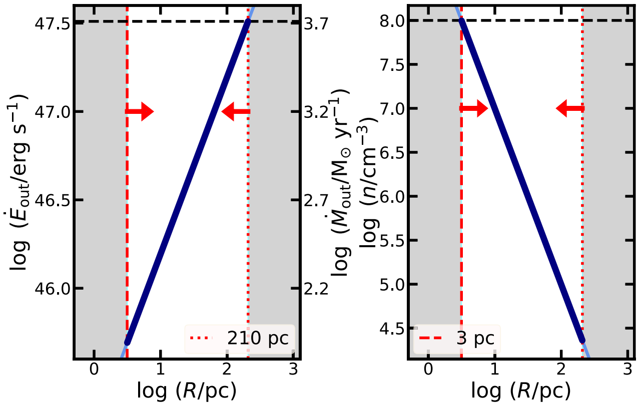

Figure 6. The range of BAL radii estimated from our analysis and the corresponding range of outflow properties. The dashed horizontal black lines represent the upper limits on the wind kinetic luminosity ($\dot{E}_{\rm out} \lesssim L_{\rm Bol}$) and the gas density, $\log(n/{\rm cm}^{-3}) \lesssim 8$, which provided us with both the upper and lower limits on the radius of the BAL outflow (vertical red dotted and dashed lines, respectively).

We found that the data did not require a less restrictive model with multiple velocity-resolved ionization parameters. In order to calculate the total column density, we first calculated column density values corrected for the covering fraction from each bin and summed the values ($\log N_{\rm H} = (\log N_{\rm H} - \log U) + \log U - \log(1 + 10^{\log a})$; Arav et al. 2005; Leighly et al. 2018; Choi et al. 2020; Green et al. 2023). Similarly, the wind energetics, such as mass outflow rate, momentum flux, and kinetic luminosity, for the BAL were computed from the sum of the values calculated for each top-hat bin.

Figure 5 shows the continuum-normalized spectra of the X-Shooter data and the best-fitting *SimBAL* model. Both spectra show the difference in the widths of the troughs between HiBALs and LoBALs. Most notably, *SimBAL* discovered a C II BAL that is blended with the Si IV trough. Initial analysis by Bischetti et al. (2023) misidentified this feature as part of the Si IV opacity (their Figure 4) because the overall apparent shapes of the blended C II/Si IV trough and C IV trough are similar. The *SimBAL* analysis revealed the presence of a C II BAL that is associated with the Al III and Mg II BALs observed at the low-velocity end. The ionization potential to create a C II ion (11.3 eV) is comparable to those of Al III (19.9 eV) and Mg II (7.6 eV), which suggests that these ions are likely found in a similar region near the hydrogen ionization front in the photoionized gas. Therefore, it is not surprising that we find observable opacity from C II at the same velocities as Al III and Mg II BALs.

A.2. Radius of BAL Outflow

As discussed in Section 2.1, the gas density ($\log n$) cannot be constrained from the spectral analysis, due to the lack of absorption lines that are sensitive to the change in $\log n$ within the bandpass. While the outflow properties are tightly coupled to the assumed density of the outflowing gas (Figure 6), the photoionized gas responsible for the BAL features in J0923+0402 can have a wide range of densities and still produce the same absorption features, as the strengths of the absorption lines observed in the data do not depend on the density of the gas. Thus, we make assumptions based on what we know about the radiatively driven outflows and BAL spectral features to provide a plausible range of BAL locations.

The upper limit on the BAL radius ($R_{\rm BAL} = 210$ pc) is derived by assuming that the BAL outflow is a steady radiatively driven wind (e.g., King & Pounds 2015; Zubovas & King 2013), requiring that the wind kinetic luminosity does not exceed $L_{\rm Bol}$. Indeed, if J0923+0402 underwent a more luminous quasar (super-Eddington accretion) phase, which is sometimes assumed for high-redshift quasars (e.g., Pezzulli et al. 2016), our upper limit may be underestimated. We derive a lower limit on $R_{\rm BAL} = 3$ pc by considering a conservative upper limit on the gas density $\log(n/{\rm cm}^{-3}) \lesssim 8$, consistent with the highest-density values measured in FeLoBAL quasars at $z \lesssim 2$ (Choi et al. 2022b). This can be done by using the best-fit U from *SimBAL*; applying the definition of the ionization parameter, $U = Q/(4\pi R_{\rm BAL}^2 nc)$, in which $\log Q = 57.2$ photons s^{-1} is the rate of photoionizing photons, estimated from the SED input to CLOUDY scaled to the $L_{3000\,\text{Å}}$ measured from the X-Shooter data (Mazzucchelli et al. 2023); and then integrating for energies greater than 13.6 eV. A significantly higher density would be similar to that of gas in the quasar BLR, and the outflowing gas could produce extra emission-line features that are not observed in the X-Shooter data (Figure 1), given the high column density. Such a limit on the radius places the BAL gas beyond the BLR, consistent with our best-fitting *SimBAL* model, where the fractions of partial coverage of the continuum and line emission by BAL outflow are the same. Moreover, we did not find evidence for an improvement in the fit when using a different covering factor for continuum and emission lines, in agreement with the BAL gas being located beyond the BLR. A relevant size scale is the inner edge of the dusty torus, often estimated from the dust sublimation radius. By using equation $R_{\rm sub} = 0.16(L_{\rm Bol}/10^{45}{\rm erg\ s}^{-1})^{1/2}$ pc (Elitzur & Netzer 2016), we find $R_{\rm sub} \sim 2.7$ pc, comparable to the lower limit on the BAL wind radius. On the other hand, the upper limit on the radius of the BAL wind is in order-of-magnitude agreement with the distance from the quasar location of the bulk of the outflowing [C II] gas ($\simeq$520 pc; Section 2.2).

Appendix B
Channel Maps of the [C II] Emission

Figure 7 shows the channel maps of the [C II] emission detected in the inner ≃5.5 kpc region around J0923+0402. These maps correspond to 30 km s^{-1} channels, spanning the velocity range between ±500 km s^{-1}, in which most of the [C II] emission is detected (Section 2.2). We find that most of the low-velocity emission is located in the region between the quasar position and the companion galaxy, whose presence is suggested by a second peak in the 242–257 GHz continuum map (Figure 2, left panel), consistent with a late merger scenario. This is also supported by the fact that we do not see an ordered kinematics in the quasar host galaxy (Figure 2, right panel). On the other hand, we find that the high-velocity, blueshifted ($v \lesssim -250$ km s^{-1}) emission is mostly located close to the quasar position, suggesting the presence of a [C II] outflow in the host galaxy.

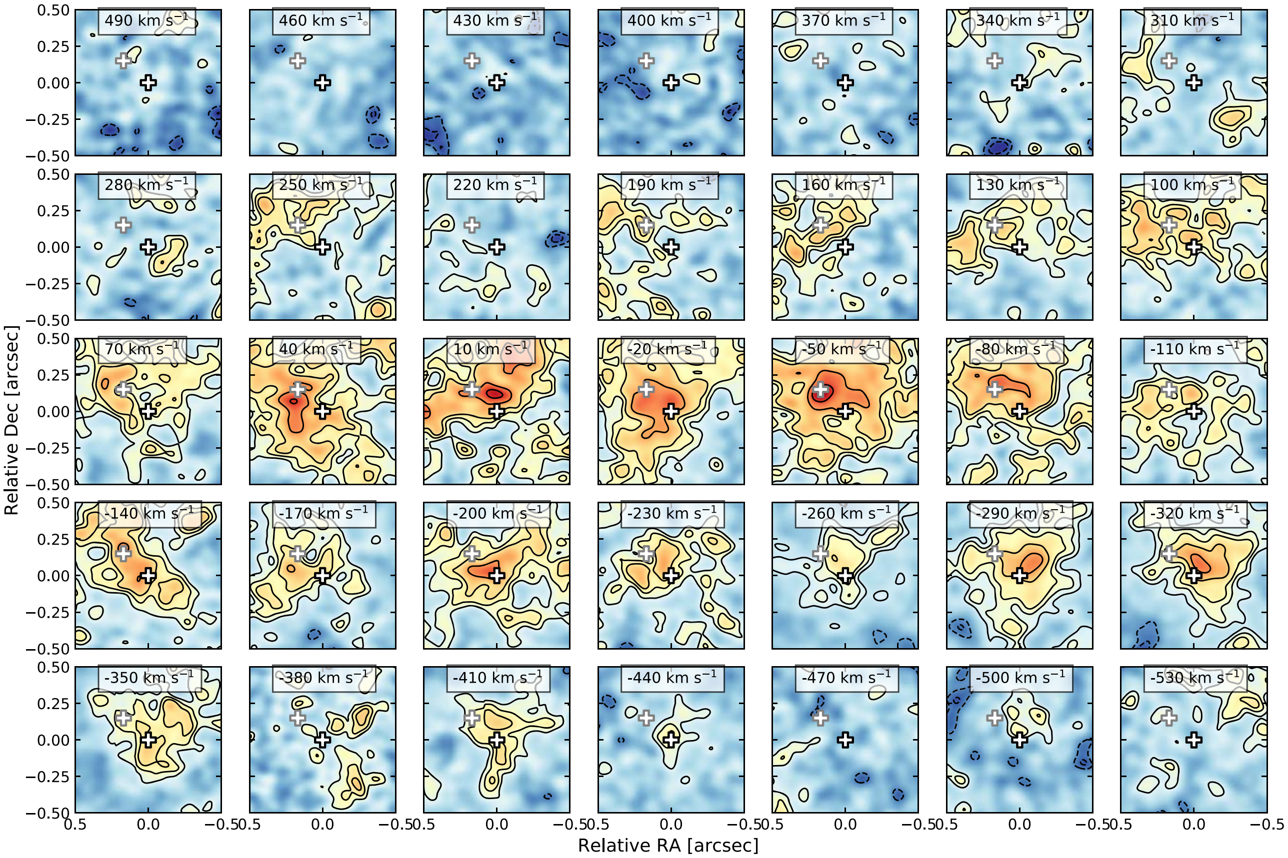

Figure 7. Channel maps of the [C II] emission in the central 1 × 1 arcsec^2 region around J0923+0402, in bins of 30 km s^{-1}. Contours correspond to [−3, −2, 2, 3, 4, 6, 8, 10]σ, where $\sigma = 7.8 \times 10^{-5}$ Jy beam^{-1}. The white plus signs mark the quasar position (black contour) and the position of the secondary peak in the continuum emission (gray contour), likely associated with a companion galaxy (Section 2.2).

ORCID iDs

Manuela Bischetti https://orcid.org/0000-0002-4314-021X
Hyunseop Choi (최현섭) https:/orcid.org/0000-0002-3173-1098
Fabrizio Fiore https://orcid.org/0000-0002-4031-4157
Chiara Feruglio https://orcid.org/0000-0002-4227-6035
Stefano Carniani https://orcid.org/0000-0002-6719-380X
Valentina D'Odorico https://orcid.org/0000-0003-3693-3091
Eduardo Bañados https://orcid.org/0000-0002-2931-7824
Huanqing Chen https://orcid.org/0000-0002-3211-9642
Roberto Decarli https://orcid.org/0000-0002-2662-8803
Simona Gallerani https://orcid.org/0000-0002-7200-8293
Julie Hlavacek-Larrondo https://orcid.org/0000-0001-7271-7340
Samuel Lai https://orcid.org/0000-0001-9372-4611
Karen M. Leighly https://orcid.org/0000-0002-3809-0051
Chiara Mazzucchelli https://orcid.org/0000-0002-5941-5214
Laurence Perreault-Levasseur https://orcid.org/0000-0003-3544-3939
Roberta Tripodi https://orcid.org/0000-0002-9909-3491
Fabian Walter https://orcid.org/0000-0003-4793-7880
Feige Wang https://orcid.org/0000-0002-7633-431X
Jinyi Yang https://orcid.org/0000-0001-5287-4242
Maria Vittoria Zanchettin https://orcid.org/0000-0001-7883-496X
Yongda Zhu https://orcid.org/0000-0003-3307-7525

References

Aalto, S., Garcia-Burillo, S., Muller, S., et al. 2012, A&A, 537, A44
Aalto, S., Garcia-Burillo, S., Muller, S., et al. 2015, A&A, 574, A85
Akins, H. B., Fujimoto, S., Finlator, K., et al. 2022, ApJ, 934, 64
Appleton, P. N., Guillard, P., Boulanger, F., et al. 2013, ApJ, 777, 66
Arav, N., Kaastra, J., Kriss, G. A., et al. 2005, ApJ, 620, 665
Arav, N., Liu, G., Xu, X., et al. 2018, ApJ, 857, 60
Astropy Collaboration, Price-Whelan, A. M., Lim, P. L., et al. 2022, ApJ, 935, 167
Astropy Collaboration, Price-Whelan, A. M., Sipőcz, B. M., et al. 2018, AJ, 156, 123
Astropy Collaboration, Robitaille, T. P., Tollerud, E. J., et al. 2013, A&A, 558, A33
Barai, P., Gallerani, S., Pallottini, A., et al. 2018, MNRAS, 473, 4003
Beelen, A., Cox, P., Benford, D. J., et al. 2006, ApJ, 642, 694
Bischetti, M., Feruglio, C., D'Odorico, V., et al. 2022, Natur, 605, 244
Bischetti, M., Fiore, F., Feruglio, C., et al. 2023, ApJ, 952, 44
Bischetti, M., Maiolino, R., Carniani, S., et al. 2019a, A&A, 630, A59
Bischetti, M., Piconcelli, E., Feruglio, C., et al. 2019b, A&A, 628, A118
Bruni, G., Piconcelli, E., Misawa, T., et al. 2019, A&A, 630, A111
Carilli, C. L., & Walter, F. 2013, ARA&A, 51, 105
Choi, H., Leighly, K. M., Dabbieri, C., et al. 2022a, ApJ, 936, 110
Choi, H., Leighly, K. M., Terndrup, D. M., et al. 2022b, ApJ, 937, 74
Choi, H., Leighly, K. M., Terndrup, D. M., Gallagher, S. C., & Richards, G. T. 2020, ApJ, 891, 53
Cicone, C., Maiolino, R., Gallerani, S., et al. 2015, A&A, 574, A14
Cicone, C., Maiolino, R., Sturm, E., et al. 2014, A&A, 562, A21
Costa, T. 2023, MNRAS, 531, 930
Costa, T., Arrigoni Battaia, F., Farina, E. P., et al. 2022, MNRAS, 517, 1767
Costa, T., Rosdahl, J., & Kimm, T. 2019, MNRAS, 489, 5181
Costa, T., Sijacki, D., Trenti, M., & Haehnelt, M. G. 2014, MNRAS, 439, 2146
Curtis-Lake, E., Bluck, A., d'Eugenio, F., Maiolino, R., & Sijacki, D. 2023, NaAs, 7, 247
Davies, R. L., Ryan-Weber, E., D'Odorico, V., et al. 2023, MNRAS, 521, 289
de Kool, M., Korista, K. T., & Arav, N. 2002, ApJ, 580, 54
Decarli, R., Dotti, M., Bañados, E., et al. 2019, ApJ, 880, 157
Decarli, R., Walter, F., Venemans, B. P., et al. 2018, ApJ, 854, 97
Dekel, A., Birnboim, Y., Engel, G., et al. 2009, Natur, 457, 451
D'Odorico, V., Bañados, E., Becker, G. D., et al. 2023, MNRAS, 523, 1399
Dunn, J. P., Crenshaw, D. M., Kraemer, S. B., & Trippe, M. L. 2010, ApJ, 713, 900
Elitzur, M., & Netzer, H. 2016, MNRAS, 459, 585
Elvis, M. 2000, ApJ, 545, 63
Farina, E. P., Arrigoni-Battaia, F., Costa, T., et al. 2019, ApJ, 887, 196
Faucher-Giguère, C.-A., & Quataert, E. 2012, MNRAS, 425, 605
Ferland, G. J., Chatzikos, M., Guzmán, F., et al. 2017, RMxAA, 53, 385
Fiore, F., Feruglio, C., Shankar, F., et al. 2017, A&A, 601, A143
Fluetsch, A., Maiolino, R., Carniani, S., et al. 2019, MNRAS, 483, 4586
Fujimoto, S., Ouchi, M., Ferrara, A., et al. 2019, ApJ, 887, 107
Fujimoto, S., Silverman, J. D., Bethermin, M., et al. 2020, ApJ, 900, 1
Gibson, R. R., Jiang, L., Brandt, W. N., et al. 2009, ApJ, 692, 758
Ginolfi, M., Jones, G. C., Béthermin, M., et al. 2020a, A&A, 633, A90
Ginolfi, M., Jones, G. C., Béthermin, M., et al. 2020b, A&A, 643, A7
Green, K. S., Gallagher, S. C., Leighly, K. M., et al. 2023, ApJ, 953, 186
Hailey-Dunsheath, S., Nikola, T., Stacey, G. J., et al. 2010, ApJL, 714, L162
Herrera-Camus, R., Förster Schreiber, N., Genzel, R., et al. 2021, A&A, 649, A31
Hewett, P. C., & Foltz, C. B. 2003, AJ, 125, 1784
Hu, H., Inayoshi, K., Haiman, Z., et al. 2022, ApJ, 935, 140
Inayoshi, K., Nakatani, R., Toyouchi, D., et al. 2022, ApJ, 927, 237
Izumi, T., Onoue, M., Matsuoka, Y., et al. 2021, ApJ, 908, 235
Janssen, A. W., Christopher, N., Sturm, E., et al. 2016, ApJ, 822, 43
Kato, N., Matsuoka, Y., Onoue, M., et al. 2020, PASJ, 72, 84
Kaufman, M. J., Wolfire, M. G., Hollenbach, D. J., & Luhman, M. L. 1999, ApJ, 527, 795
King, A., & Pounds, K. 2015, ARA&A, 53, 115
Lagache, G., Cousin, M., & Chatzikos, M. 2018, A&A, 609, A130
Lambert, T. S., Posses, A., Aravena, M., et al. 2023, MNRAS, 518, 3183
Leibler, C. N., Cantalupo, S., Holden, B. P., & Madau, P. 2018, MNRAS, 480, 2094
Leighly, K. M., Terndrup, D. M., Gallagher, S. C., Richards, G. T., & Dietrich, M. 2018, ApJ, 866, 7
Leighly, K. M., Terndrup, D. M., Lucy, A. B., et al. 2019, ApJ, 879, 27
Lucy, A. B., Leighly, K. M., Terndrup, D. M., Dietrich, M., & Gallagher, S. C. 2014, ApJ, 783, 58
Lutz, D., Sturm, E., Janssen, A., et al. 2020, A&A, 633, A134
Maddox, N., Hewett, P. C., Warren, S. J., & Croom, S. M. 2008, MNRAS, 386, 1605
Maiolino, R., Cox, P., Caselli, P., et al. 2005, A&A, 440, L51
Maiolino, R., Gallerani, S., Neri, R., et al. 2012, MNRAS, 425, L66
Marconi, A., Risaliti, G., Gilli, R., et al. 2004, MNRAS, 351, 169
Marshall, M. A., Perna, M., Willott, C. J., et al. 2023, A&A, 678, A191
Matsuoka, Y., Iwasawa, K., Onoue, M., et al. 2018, ApJS, 237, 5
Mazzucchelli, C., Bischetti, M., D'Odorico, V., et al. 2023, A&A, 676, A71
Menci, N., Fiore, F., Feruglio, C., et al. 2019, ApJ, 877, 74
Meyer, R. A., Walter, F., Cicone, C., et al. 2022, ApJ, 927, 152
Miller, T. R., Arav, N., Xu, X., & Kriss, G. A. 2020, MNRAS, 499, 1522
Neeleman, M., Novak, M., Venemans, B. P., et al. 2021, ApJ, 911, 141
Novak, M., Venemans, B. P., Walter, F., et al. 2020, ApJ, 904, 131
Obreja, A., Arrigoni Battaia, F., Macciò, A. V., & Buck, T. 2024, MNRAS, 527, 8078
Pallottini, A., Ferrara, A., Gallerani, S., Salvadori, S., & D'Odorico, V. 2014, MNRAS, 440, 2498
Pezzulli, E., Valiante, R., & Schneider, R. 2016, MNRAS, 458, 3047
Pizzati, E., Ferrara, A., Pallottini, A., et al. 2023, MNRAS, 519, 4608
Planck Collaboration, Ade, P. A. R., Aghanim, N., et al. 2016, A&A, 594, A13
Ramos Almeida, C., Bischetti, M., García-Burillo, S., et al. 2022, A&A, 658, A155
Richings, A. J., & Faucher-Giguère, C.-A. 2018, MNRAS, 474, 3673
Sabra, B. M., & Hamann, F. 2005, arXiv:astro-ph/0509421
Schindler, J.-T., Farina, E. P., Bañados, E., et al. 2020, ApJ, 905, 51
Somerville, R. S., & Davé, R. 2015, ARA&A, 53, 51
Speranza, G., Ramos Almeida, C., Acosta-Pulido, J. A., et al. 2023, A&A, 681, A63
Stern, J., Sternberg, A., Faucher-Giguère, C.-A., et al. 2021, MNRAS, 507, 2869
Tripodi, R., Feruglio, C., Fiore, F., et al. 2022, A&A, 665, A107
Tripodi, R., Feruglio, C., Kemper, F., et al. 2023, ApJL, 946, L45
Tripodi, R., Scholtz, J., Maiolino, R., et al. 2024, A&A, 682, A54
Tumlinson, J., Peeples, M. S., & Werk, J. K. 2017, ARA&A, 55, 389
Valentini, M., Gallerani, S., & Ferrara, A. 2021, MNRAS, 507, 1
Vallini, L., Gallerani, S., Ferrara, A., Pallottini, A., & Yue, B. 2015, ApJ, 813, 36
van der Vlugt, D., & Costa, T. 2019, MNRAS, 490, 4918
Venemans, B. P., Walter, F., Neeleman, M., et al. 2020, ApJ, 904, 130

Vietri, G., Misawa, T., Piconcelli, E., et al. 2022, A&A, 668, A87
Vito, F., Di Mascia, F., Gallerani, S., et al. 2022, MNRAS, 514, 1672
Volonteri, M. 2012, Sci, 337, 544
Wang, F., Yang, J., Fan, X., et al. 2019, ApJ, 884, 30
Yang, J., Wang, F., Fan, X., et al. 2021, ApJ, 923, 262
Zanchettin, M. V., Feruglio, C., Bischetti, M., et al. 2021, A&A, 655, A25
Zanchettin, M. V., Feruglio, C., Massardi, M., et al. 2023, A&A, 679, A88
Zubovas, K., & King, A. 2012, ApJL, 745, L34
Zubovas, K., & King, A. 2013, ApJ, 769, 51
Zubovas, K., & King, A. 2021, MNRAS, 501, 4289
Zubovas, K., & Maskeliūnas, G. 2023, MNRAS, 524, 4819